MIT Open Access Articles

ExoplanetSat: Detecting transiting exoplanets using a low-cost CubeSat platform

Citation	Smith, Matthew W. et al. "ExoplanetSat: detecting transiting exoplanets using a low-cost CubeSat platform." Space Telescopes and Instrumentation 2010: Optical, Infrared, and Millimeter Wave. Ed. Jacobus M. Oschmann et al. San Diego, California, USA: SPIE, 2010. 773127-14. © 2010 SPIE
As Published	http://dx.doi.org/10.1117/12.856559
Publisher	SPIE
Version	Final published version
Accessed	Mon Feb 19 20:49:11 EST 2018
Citable Link	http://hdl.handle.net/1721.1/61644
Terms of Use	Article is made available in accordance with the publisher's policy and may be subject to US copyright law. Please refer to the publisher's site for terms of use.
Detailed Terms	

ExoplanetSat: Detecting transiting exoplanets using a low-cost CubeSat platform

Matthew W. Smith[a], Sara Seager[b], [d], Christopher M. Pong[a], Jesus S. Villaseñor[c],
George R. Ricker[c], David W. Miller[a], Mary E. Knapp[a], Grant T. Farmer[b],
Rebecca Jensen-Clem[d]

[a]Department of Aeronautics and Astronautics
[b]Department of Earth, Atmospheric and Planetary Sciences
[c]Kavli Institute for Astrophysics and Space Research
[d]Department of Physics
Massachusetts Institute of Technology, 77 Massachusetts Ave, Cambridge, MA 02139

ABSTRACT

Nanosatellites, i.e. spacecraft that weigh between 1 and 10 kg, are drawing increasing interest as platforms for conducting on-orbit science. This trend is primarily driven by the ability to piggyback nanosatellites on the launch of large spacecraft and hence achieve orbit at greatly reduced cost. The CubeSat platform is a standardized nanosatellite configuration, consisting of one, two, or three 10 cm x 10 cm x 10 cm units (1, 2, or 3 "U"s) arranged in a row. We present a CubeSat-based concept for the discovery of transiting exoplanets around the nearest and brightest Sun-like stars. The spacecraft prototype—termed ExoplanetSat—is a 3U space telescope capable of monitoring a single target star from low Earth orbit. Given the volume limitations of the CubeSat form factor, designing a capable spacecraft requires overcoming significant challenges. This work presents the initial satellite configuration along with several subsystem-specific solutions to the aforementioned constraints. An optical design based on a modified commercial off-the-shelf camera lens is given. We also describe a novel two-stage attitude control architecture that combines 3-axis reaction wheels for coarse pointing with a piezoelectric translation stage at the focal plane for fine pointing. Modeling and simulation results are used to demonstrate feasibility by quantifying ExoplanetSat pointing precision, signal-to-noise ratio, guide star magnitude, and additional design parameters which determine system performance.

Keywords: Exoplanets, transit detection method, CubeSat, nanosatellite, jitter noise, photometric precision.

1. INTRODUCTION

The detection and characterization of exoplanets—i.e. planets orbiting stars outside our solar system—is a recent and very active area of astronomy. Hundreds of exoplanets have been discovered since the mid-1990s, however the majority of these planets are gas giants (see Figure 1). Given the expected composition and temperatures of such exoplanets, it is highly unlikely that the planets discovered so far can support life. The current "holy grail" of the search for exoplanets is a true Earth analog: an Earth-like (i.e. small, rocky) planet orbiting in the habitable zone of a Sun-like star. The habitable zone is the orbital region in which temperatures allow water to exist in liquid form on the surface of a planet. As of yet, no missions have discovered these Earth analogs. A mission designed to detect Earths can also more easily detect larger or more massive planets in more favorable orbits.

ExoplanetSat is a miniature space telescope, currently in the conceptual design phase, intended to detecting Earth-like planets orbiting nearby bright Sun-like stars. This work describes the spacecraft baseline and initial feasibility analysis. Once a single ExoplanetSat prototype has flown successfully, replicated fabrication will produce subsequent copies based on the demonstrated design. This will allow for the monitoring of multiple target stars simultaneously.

Further author information: (Send correspondence to M. Smith)
M. Smith: m_smith@mit.edu
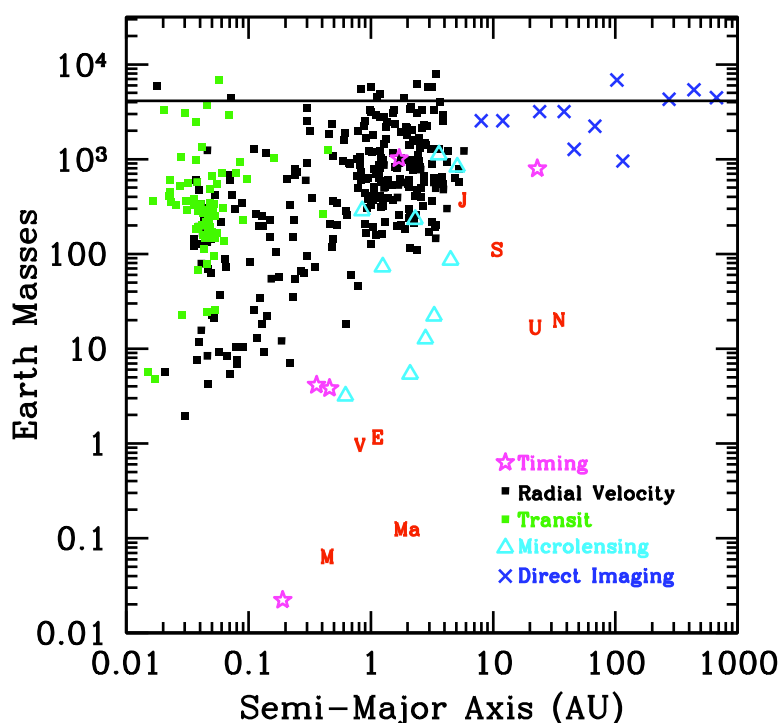S. Seager: seager@mit.edu
C. Pong: cpong@mit.edu

Figure 1. Known exoplanets plotted according to mass and semi-major orbital axis (normalized by Earth) and detection method. Data from [http://exoplanets.eu/].

1.1 Science case

Several methods exist for detecting exoplanets, with radial velocity measurements being the approach that has yielded the most detections. However, physical characterization of exoplanet atmospheres is desirable and not possible with radial velocity measurements alone. Atmosphere observations can potentially lead to the identification of biosignature gases or habitability indicators (e.g. water vapor, methane, carbon dioxide, oxygen, etc).[1] A requirement for physical characterization of exoplanet atmospheres points either to direct imaging or the transit method. Although proposed coronagraph[2] and interferometric[3] concepts exist for directly detecting and characterizing exoplanets (e.g. Terrestrial Planet Finder[4,5]), a lack of technological maturity puts these missions in the future.

The transit method therefore provides a second path to the discovery and characterization of Earth-like exoplanets in the near term. A subset of exoplanets cross in front of their stars as seen from Earth ("primary eclipse" or "transit"). When the planet transits the star as seen from Earth, the starlight gets dimmer by the planet-to-star area ratio. If the size of the star is known, the planet size can be derived. The transit technique also makes it possible to characterize atmospheric constituents of exoplanets. During the planet transit, some of the starlight passes through the optically thin part of the planet atmosphere, picking up spectral features from the planet. A planetary transmission spectrum can be obtained by dividing the spectrum of the star and planet during transit by the spectrum of the star alone (i.e. before or after transit). In this way there is a potential to study atmospheres of Earth analogs, provided the star is bright enough. Highlights of such observations of hot giant exoplanets include the discovery of sodium in HD 209458b[6] and water and methane in HD 189733.[7,8]

The ExoplanetSat spacecraft will attempt to detect exoplanets using the transit method. Once a detection occurs, the parent star will become a high-priory target for follow-on observations. Such a follow-up is only possible if the star is sufficiently bright, therefore ExoplanetSat will target the nearest and brightest (approximately $0 < V < 5$) Sun-like stars in the sky. Because the brightest stars are too widely separated across the sky for a

single telescope field of view to continuously monitor, ExoplanetSat will use a targeted search, as described in Section 1.3. The ultimate goal is a fleet of many ExoplanetSats, each monitoring a different target star.

1.2 Prior work and related missions

CubeSats are a class of nanosatellites initially developed at Stanford University and California Polytechnic State University, San Louis Obispo to facilitate low-cost access to space.[9] This is primarily accomplished by the small size of a single CubeSat unit ("U"), which measures 10 cm on a side and has a mass of 1.33 kg.[10] CubeSats are launched as piggyback secondary payloads on large launch vehicles using the Poly-Picosatellite Orbital Deployer (P-POD)—a tube-like containment box attached to the launch vehicle that holds up to three 1U CubeSats and releases them upon reaching orbit.[11] ExoplanetSat is a triple-CubeSat measuring 10 cm × 10 cm × 34 cm. By adopting the standardized CubeSat form factor, ExoplanetSat is compatible with the (P-POD), which affords many more launch opportunities at lower cost than would be possible with a larger or non-standardized configuration. Furthermore, the CubeSat specification means greater compatibility with a range of commercial off-the-shelf (COTS) components.

Imaging satellites based on the CubeSat bus have been implemented for Earth-observing missions. The Miniature Imaging Spacecraft (MISC) developed by Pumpkin, Inc. is a 3U space telescope designed to provide low-cost multispectral imagery from a 540 km circular orbit.[12] While the application is different from that of ExoplanetSat, the baseline spacecraft configuration—a three-axis stabilized, 3U CubeSat with an optical payload and deployable solar arrays—is similar. Recently, the United States government has sought to use CubeSats as low-cost platforms for advanced technology development, including hyperspectral sensors.[13]

There are several space telescope missions relevant to the search for exoplanets. Launched in 2006, the Convection, Rotation and planetary Transits (CoRoT) spacecraft is a small space telescope with a roughly 0.3 m diameter primary mirror.[14] CoRoT is a mission of the French space agency (CNES) designed to conduct astroseismoloy measurements and detect transiting exoplanets by observing approximately 12,000 target stars simultaneously during 5 month periods. The mission aims to achieve a photometric precision of 7×10^{-4} for $V = 15.5$ mag stars over a one-hour integration[15] and has detected fourteen exoplanets thus far.[16]

The Microvariability and Oscillations of Stars (MOST) mission is another high photometric-precision space telescope for astroseismology and exoplanet transit observations.[17, 18] The MOST spacecraft is especially relevant to ExoplanetSat given its low volume (65 cm × 65 cm × 30 cm) and low mass (54 kg). MOST uses unique optical setup wherein light from the target star is deliberately positioned on a field stop. This places an image of the telescope entrance pupil on the science CCD, minimizing the impact of pixel-to-pixel response variations and subpixel variations.

Finally, NASA's Kepler spacecraft—launched in March 2009—is arguably the flagship exoplanet mission currently in operation. Residing in an Earth-trailing heliocentric orbit, Kepler uses a highly precise CCD photometer to monitor transiting terrestrial planets around a field of roughly 150,000 main sequence stars.[19] The goal of this mission is to provide a census of Earths, i.e. to measure the frequency of Earth-sized planets in Earth-like orbits around Sun-like stars. In order to accomplish this, Kepler uses a large field of view to observe many faint stars. However because the stars are so faint, transit atmosphere measurements for small planets will not be possible.

1.3 Concept of operations

Each ExoplanetSat spacecraft will monitor a single bright star, therefore monitoring a variety of candidates will require a collection of identical spacecraft in orbit simultaneously. From a low-inclination low Earth orbit (LEO) at approximately 650 km altitude, each ExoplanetSat will observe its target star when visible during orbital night. Observation during orbital day is precluded due to thermal, power, and lighting constraints. An Earth-twin transit across the center of a star would last 13 hours, thus the observing cadence from low-inclination LEO (i.e. roughly 30 minutes of orbital night followed by roughly 60 minutes of orbital day) is sufficient to detect such an event. During orbital dawn, the spacecraft will reorient itself to point the solar panels toward the Sun. Likewise, during orbital dusk the spacecraft will slew to re-acquire the target star.

1.4 Photometry requirements and noise

The requirement on photometric precision needed to detect an Earth analog drives the design of ExoplanetSat. The depth of a transit, i.e. the amount by which the target star brightness decreases during an exoplanet primary eclipse, is determined by the planet-to-star area ratio. An Earth-sized planet transiting a Sun-sized star has a transit depth of 8.4×10^{-5}. Therefore the ExoplanetSat payload must be able to detect a roughly 1 part in 10,000—or 100 part per million (ppm)—reduction in stellar brightness. To ensure confidence in a potential detection, we require a 7σ limit on the system noise. Therefore total error in the photometric signal σ_{tot} must be less than $(100 \text{ ppm})/7 = 14.3$ ppm. For margin, the requirement on total photometric noise is set at 10 ppm. For the purposes of this work, this is considered to be over an individual observation lasting on the order of hundreds of seconds. We actually require this precision over an entire transit (approximately 13 hours for an Earth/Sun pair), which will contain many separate observations, therefore the above requirement is conservative.

For the purposes of this study, the total photometric noise is decomposed into noise from the CCD detector, σ_{CCD} and noise on the signal due to high frequency spacecraft motion (i.e. "jitter"), σ_{jitter}. Because these two noise sources are independent and random, they combine in quadrature in the usual fashion:

$$\sigma_{\mathrm{tot}} = \sqrt{\sigma_{\mathrm{CCD}}^2 + \sigma_{\mathrm{jitter}}^2} \ \leq 10 \text{ ppm}. \tag{1}$$

Detector and jitter noise are discussed in Sections 3.1 and 3.2 along with related simulation results and analysis.

2. BUS OVERVIEW

The core bus subsystems—power, avionics, communications, structure, thermal, and attitude determination and control (ADCS)—have been baselined to differing levels of detail. Where possible, we seek to use COTS components developed for the CubeSat community. Figure 2 shows the baseline configuration of the ExoplanetSat spacecraft.

2.1 Power

Power will nominally be supplied by a set deployable solar arrays. The current baseline arrangement is the "cross" configuration shown in Figure 3a. Here four 10 cm × 30 cm deployed panels face the direction opposite the lens. There is also a single 10 cm × 10 cm panel at the center of the cross. Nominal power production from the cross configuration is 31 W. An alternative arrangement is the "table" configuration shown in Figure 3b. Here five 10 cm × 30 cm panels (four deployed, one body-mounted) form a surface that generates 36.5 W. The table configuration is advantageous because it offers additional power margin and the geometry of the panels with respect to the optics prevents the lens from viewing the Earth during orbital daylight, which can heat the detector. Also, the spacecraft must reorient itself during each orbital dawn and dusk, and the table configuration results in smaller slew maneuvers. However, the table deployment mechanism is under development while the cross-style hinges are available, thus the cross is the baseline configuration. The average power required during orbital night is approximately 17.6 W, which accounts for operating the attitude control subsystem (reaction wheels, piezo stage, torque coils), science detector, avionics, and communications. Note that this power is drawn from the batteries, given that the solar panels are not illuminated. The average power required from the solar panels during orbital day is 28.5 W, which accounts for the attitude control subsystem, avionics, communications, and battery charging.

In both configurations the arrays are COTS components produced by Clyde Space (panels and cells) and Pumpkin, Inc. (spring-loaded hinges). The arrays will lie flat against the spacecraft while in the P-POD and passively spring open upon release from the carrier. During orbital daylight, the spacecraft will be oriented so that the deployed solar cells directly face the Sun, maximizing the charging rate. In addition to the deployed solar panels, the spacecraft will have a set of body-mounted 10 cm × 30 cm solar panels. The purpose of these body-mounted cells is to provide power during spacecraft de-tumbling after deployment or in the event of a loss of attitude control. Power will be regulated by an Electrical Power Subsystem (EPS) board from Clyde Space and stored by a bank of 8 lithium-cobalt cells.
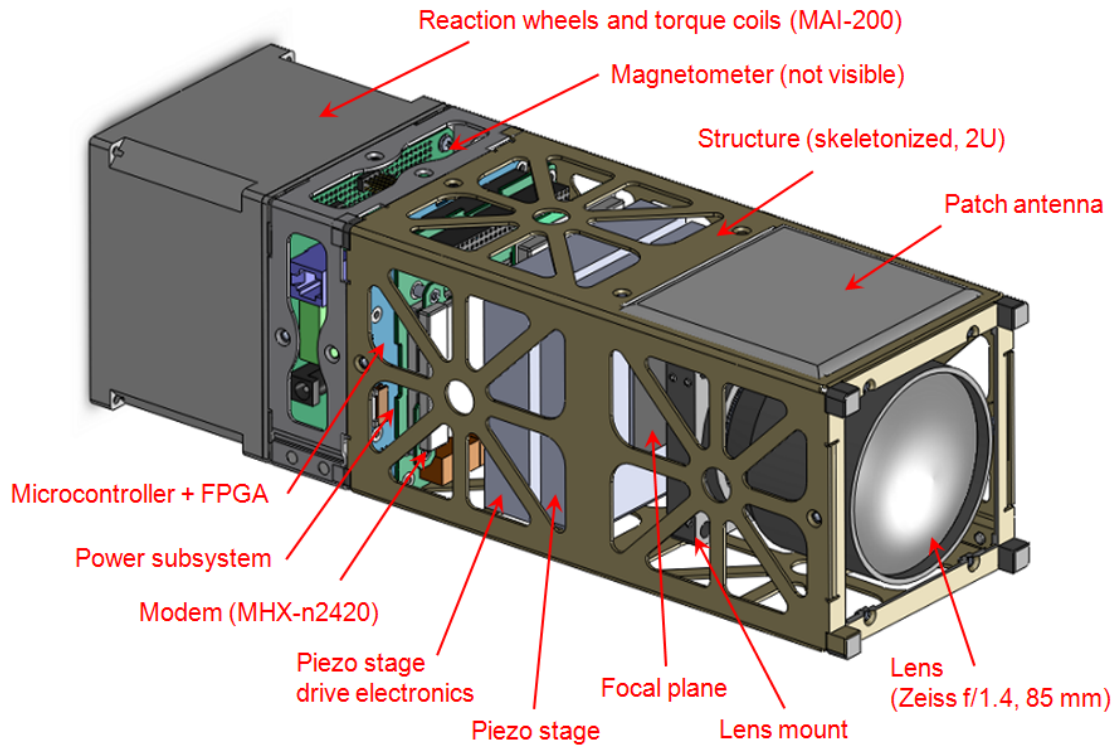
Figure 2. Baseline ExoplanetSat configuration. Not shown are the solar arrays, batteries, the light seal between the lens mount and focal plane array, and the CCD cooling strap.
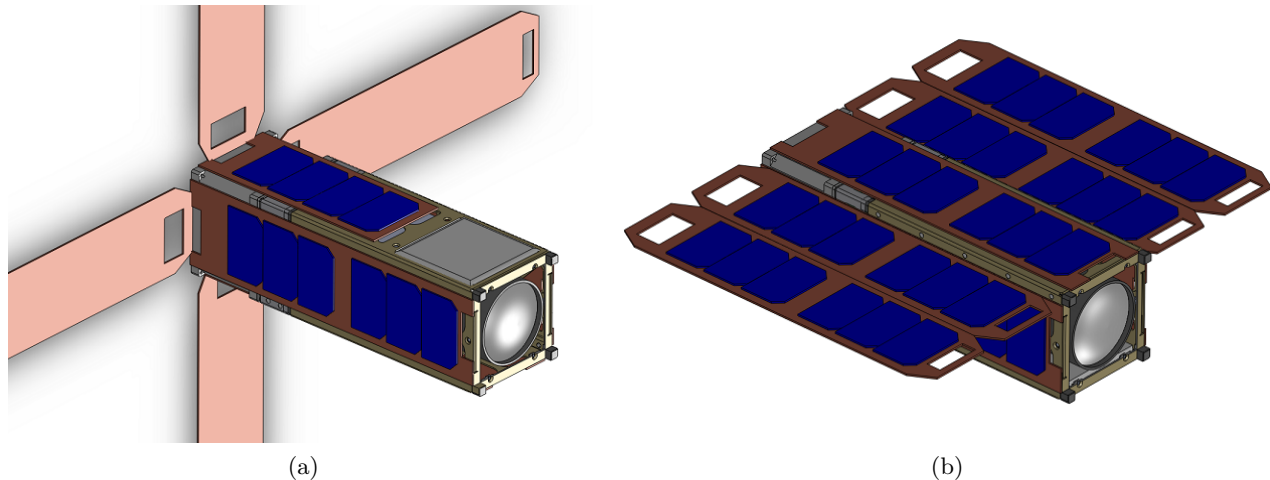

(a)   (b)

Figure 3. Possible deployable solar array configurations: (a) "cross" configuration (solar cells on the deployed panels are facing away) and (b) "table" configuration. In both cases body-mounted panels are used for tumbling scenarios.

2.2 Avionics

The avionics subsystem will be responsible for running the attitude control loop, which requires rapidly reading images from the focal plane array, performing a star tracking algorithm, performing estimation via a Kalman filter, and commanding the various actuators (see Section 2.5 below). The image processing task is a main driver

of avionics architecture. The initial design calls for a FPGA to read and process image data at a high rate. A PIC32 microcontroller will augment the FPGA and provides computing for the attitude control loop, along with communications handling and housekeeping functions. ExoplanetSat will use flash memory to store science and telemetry data for later transmission to the ground, and SDRAM for temporary storage of image data being processed by the FPGA.

2.3 Communications

The communications subsystem will use a single S-band modem, an 8 dBi patch antenna, and a 3 dBi whip antenna. The baseline transmitter/reciever is the Microhard n2420 2.4 GHz spread spectrum wireless modem, which offers the necessary functionality in a compact package (32 mm × 51 mm × 6.35 mm, 19 g). The patch antenna is used to support a high rate channel for transmitting science data to the ground. The lower gain antenna is used during the commissioning phase when precise pointing has yet to be established, or during contingencies in which attitude control is lost. ExoplanetSat will use the existing ground stations developed by MIT and international partners for the High Energy Transient Explorer (HETE-II) mission.[20] These are located along a roughly equatorial ground track in Kwajalein (Micronesia), Singapore, and Cayenne (French Guiana).

2.4 Structure and thermal

ExoplanetSat will use a modified COTS structure that consists of a 2U skeletonized aluminum cage. The electronics boards are mounted to rails that run down the interior of the cage, while custom-designed mounts affix the piezo stage (described below). A COTS mount holds the lens a fixed distance from the focal plane. Solar panels are mounted to the exterior of the structure. Thermal control is entirely passive, given the power, volume, and mass constraints. The most thermally-critical component is the science CCD detector, which must remain cool in order to minimize dark current noise. Thermal control strategies for the CCD are currently under review, however the most promising solution is the use of a thermally conductive cooling strap run between the CCD and the cavity around the lens. This space-facing cavity would then act as a radiator to passively cool the detector.

2.5 Attitude determination and control

In order to meet ExoplanetSat's stringent photometry requirement, the target star image must be stationary on the focal plane array. As discussed in Section 3.2 below, any significant motion of the star image will result in a change in the signal due to pixel gain non-uniformity, resulting in additional noise. The spacecraft pointing must therefore be controlled to a high degree of precision. To accomplish this, ExoplanetSat uses a two-stage pointing control scheme wherein reaction wheels serve as a coarse stage—controlling the spacecraft attitude to approximately 60 arcseconds (3σ) in all three axes. Residual pointing errors down to the arcsecond level are removed by a two-axis piezoelectric nanopositioning stage, on which the focal plane is mounted. The piezoelectric stage translates in the plane of the detector in order to keep the target star located on the same set of pixels. The baseline reaction wheel unit is the MAI-200, which also includes three-axis magnetic torque coils for desaturation. Centroid tracking on the focal plane and rate information from gyros will be the primary sensor outputs. See Pong *et al.*[21] for an in-depth discussion and analysis of the ExoplanetSat attitude determination and control subsystem.

3. OPTICAL PAYLOAD

The ExoplanetSat optical payload consists of a commercially available single lens reflex (SLR) camera lens and a composite focal plane array made up of a single CCD detector surrounded by tiled CMOS detector chips (see Figure 4).

The lens selection process took into account several competing design parameters. Photon collection capability is a primary consideration given the photometric nature of the mission, hence large aperture (i.e. low f-number) lenses were given priority. Because the aperture diameter increases with focal length for a constant f-number, longer focal length lenses were also prioritized. Volume limitations were also a concern, with the outer diameter of the lens being no larger than 9 cm in order to maintain volume margin in the 10 cm CubeSat envelope. For this same reason, only 35 mm format lenses were considered. Medium format lenses have a larger light spot and

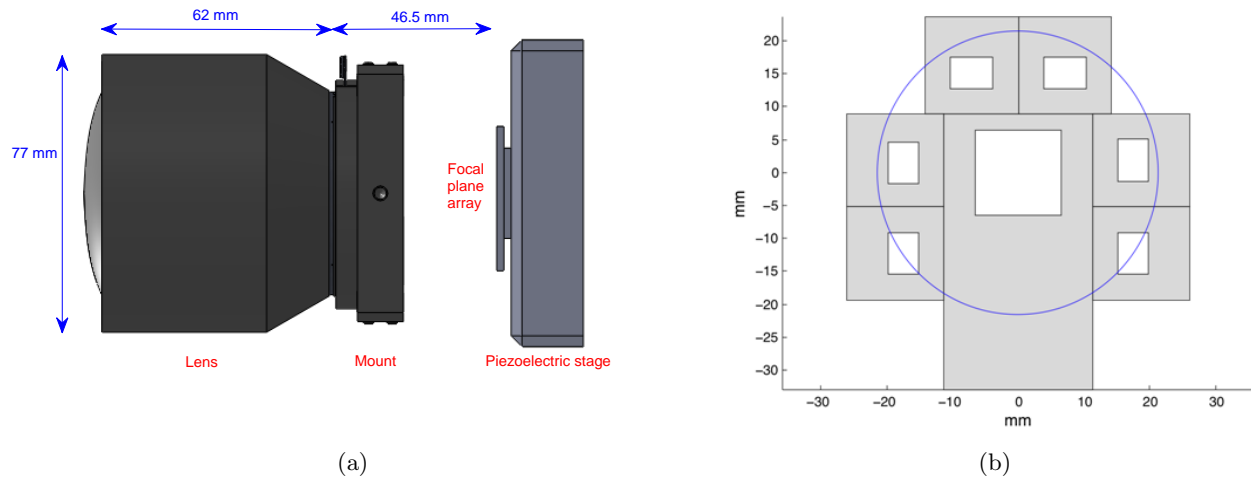(a)   (b)

Figure 4. (a) Layout of the optical payload. Note that the lens flange is one flange focal distance (FFD, 46.5 mm) away from the focal plane array, which is mounted to the piezoelectric stage. For clarity, the light seal between the lens mount and focal plane array has been removed. (b) Layout of the CCD science detector (center) and CMOS guide detectors on the focal plane. The blue circle is the extent of the lens light spot. White shows the detector area while gray shows the surrounding electronics.

therefore provide additional focal plane area and reduced vignetting. However, the flange focal distance (FFD, the distance from lens mount to image plane) on medium format lenses is much larger than for 35 mm format lenses, making the entire lens assembly prohibitively large. For example, a Nikon F-mount lens has a 46.5 mm FFD, while for a Hasselblad medium format lens the FFD is 74.9 mm. See Table 1 for a comparison of candidate lenses.

Table 1. Lenses considered for the ExoplanetSat mission, listed by light throughput (i.e. aperture area). Values are taken from manufacturers' data sheets. Lens 1 is the current baseline.

ID	Maker	Lens	f [mm]	f/#	Area* [mm²]	Length† [mm]	FFD‡ [mm]	Dia§ [mm]	Mass [g]	Cost¶ [$K]
1	Zeiss	Planar T 1.4/85	85	1.4	2895	62	46.5	77	570	1
2	Leica	Noctilux-M 50 mm f/0.95	52.3	0.95	2380	75	27.8	73	700	10
3	Leica	Apo-Summicron 90 mm f/2	90	2.0	1622	78	27.8	64	500	3.5
4	Zeiss	Sonnar T 2/85	85	2.0	1419	82	27.8	65	450	2.9
5	Zeiss	Planar T 1.4/50	50	1.4	1002	45	46.5	66	330	0.55

*Aperture area, given the effective aperture diameter computed from the focal length and f-number.
†Physical lens length.
‡Flange focal distance (i.e. distance from lens mount to image plane).
§Maximum outer lens diameter.
¶Off-the-shelf-cost (does not include modifications to flight qualify).

With these consideration in mind, the baseline choice is a Zeiss Planar T f/1.4, 85 mm F-mount lens. It offers superior optical throughput (as given by the aperture area), with only moderate volume, mass, and cost. The lens will be undergo modifications to make it space-worthy, including fixing the focus at infinity and aperture at f/1.4, removing volatile greases and cements, and venting of air spaces. The selected lens has the advantage of having previously undergone these modifications for another space application.[22]

As shown in Figure 4(b), the focal plane array consists of a single science frame-transfer CCD surrounded by multiple CMOS detectors. The CCD performs the photometry function, conducting relatively long integrations (up to 10 seconds) to collect as many photons as possible from the target star. The CMOS senors are used to track the centroids of surrounding guide stars at a much faster update rate, serving as a star tracker for attitude determination. Final component selection is ongoing, however in general the CCD will be a back-illuminated 1K $\times$ 1K array of approximately 15 μm pixels with a well capacity on the order of 100K electrons. We are currently evaluating a back-illuminated 2.6K $\times$ 1.9K CMOS sensor with 1.4 μm pixels to serve as the guide detector.

3.1 CCD detector noise

Recalling the noise equation (1), we separate the CCD noise σ_{CCD} into the three dominant components: photon (shot) noise, dark current noise, and read noise,

$$\sigma_{\mathrm{CCD}}^2 = \sigma_{\mathrm{shot}}^2 + \sigma_{\mathrm{dark}}^2 + \sigma_{\mathrm{read}}^2. \tag{2}$$

The arrival of signal photons on the detector is governed by Poisson statistics, hence the shot noise is simply,

$$\sigma_{\mathrm{shot}}^2 = S \cdot t_{\mathrm{int}} \quad [\mathrm{photons}] \tag{3}$$

where S [photons/s] is the star signal and t_{int} [s] is the integration time for that particular frame. The dark current noise is also a Poisson process, so the statistics are the same:

$$\sigma_{\mathrm{dark}}^2 = D \cdot t_{\mathrm{int}} \quad [\mathrm{photons}] \tag{4}$$

where D [photons/s] is the dark current signal. Finally, read noise is typically given in terms of RMS electrons per read, therefore the read noise for the entire frame is,

$$\sigma_{\mathrm{read}}^2 = N \cdot R^2 \quad [\mathrm{e\text{-}}] \tag{5}$$

where R [e- RMS/pixel] is the read noise value and N is the number of pixels being read.

Given these noise sources, one can express the CCD noise in ppm as the inverse of the signal-to-noise ratio (SNR):

$$\sigma_{\mathrm{CCD}} = \frac{\sqrt{F} \cdot \sigma_{\mathrm{CCD}} \ [\mathrm{photons}]}{F \cdot S \cdot t_{\mathrm{int}} \ [\mathrm{photons}]} \cdot 10^6 \quad [\mathrm{ppm}]$$

where F is the number of frames co-added over the course of a single observation point. From equations (2) through (5) the numerator can be expanded give an expression for CCD noise in ppm as a function of the parameters t_{int}, D, F, and R,

$$\sigma_{\mathrm{CCD}} = \frac{\sqrt{S t_{\mathrm{int}} + D t_{\mathrm{int}} + N R^2}}{\sqrt{F} \cdot S \cdot t_{\mathrm{int}}} \cdot 10^6 \quad [\mathrm{ppm}] \tag{6}$$

Figure 5 shows CCD noise as a function of integration time for stars of varying brightness ($M_V = 0, 4, 7$) and different amounts of co-adding. We assume a 100 $\times$ 100 pixel postage-stamp around the target star and an aperture diameter of 60.7 mm (lens 1 in Table 1). The dark current is 12.5 [e-/pixel/s] and the read noise is 2 [e-RMS]. The longest observation shown is 17 minutes (100 co-added frames at 10 s each), which accords with the available observing time during orbital night in LEO. The photometry requirement is reachable for 0 magnitude stars, however it is more difficult at 4th magnitude. Still, Figure 5b shows that by lengthening the integration time slightly and increasing F, it will be possible to reduce CCD noise further, likely to a level below the 10 ppm threshold.
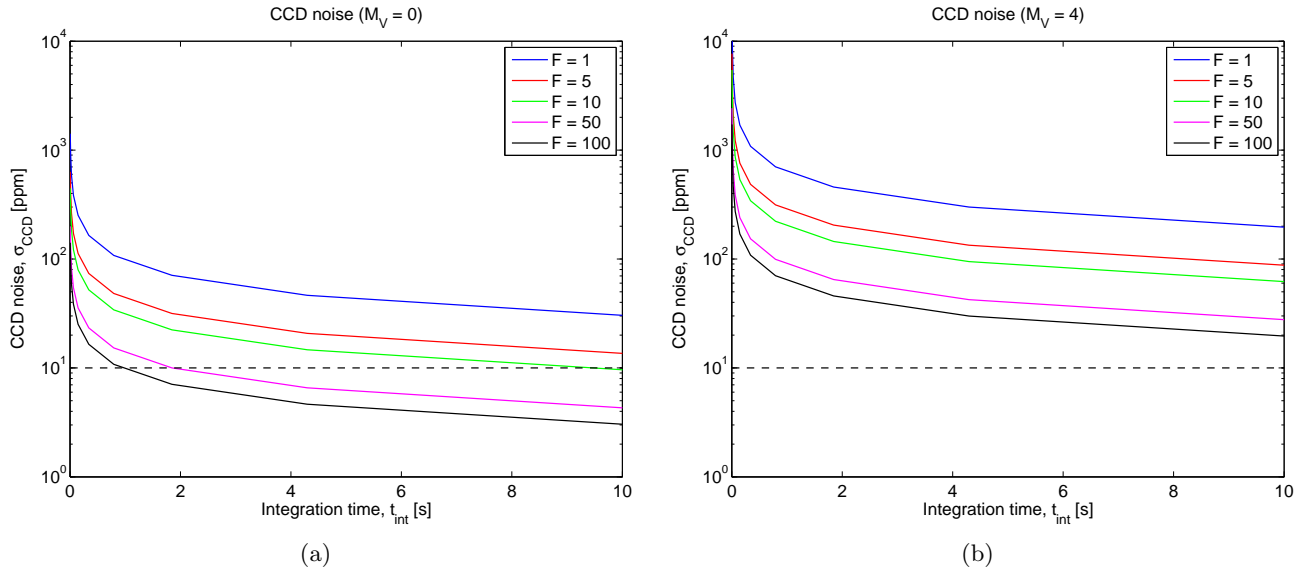
Figure 5. CCD noise as a function of integration time and number of co-added frames for (a) 0th magnitude and (b) 4th magnitude target stars. The integration time per frame is given by t_{int} while the number of frames per exposure is F.

3.2 Jitter noise

In addition to the CCD noises described above, the photometric signal will be corrupted by jitter noise, which arises due to the combination of pixel response non-uniformity (PRNU) and spacecraft pointing error. This is shown schematically in Figure 6, which depicts a defocused light spot falling on detector pixels with varying response. As the spot translates due to spacecraft jitter, a new set of pixels is covered, which—due to response variations—changes the photometric signal when the pixels are summed.
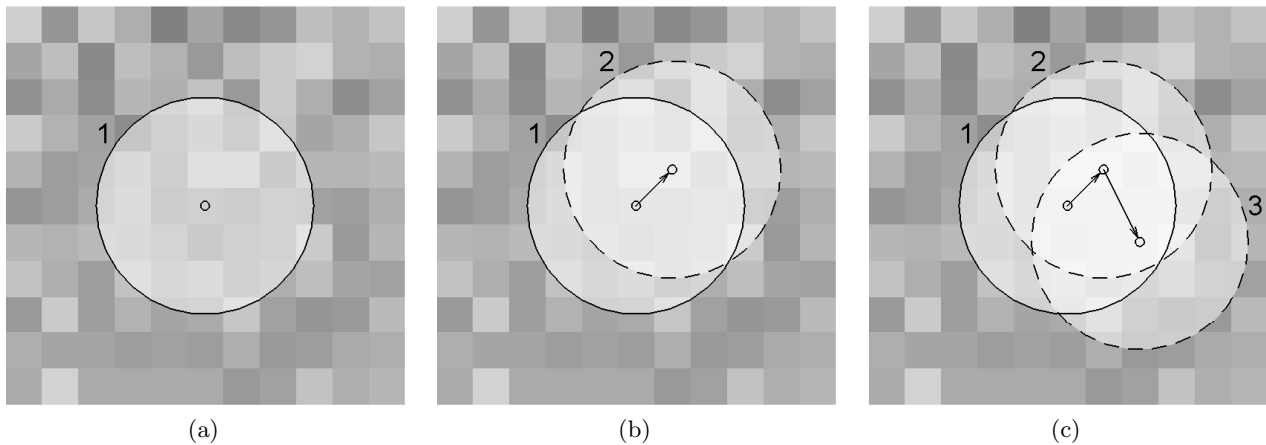

Figure 6. Schematic representation of jitter noise due to photo response non-uniformity (PRNU) and spot motion: (a) Light spot falling on pixels with gain non-uniformity, (b) shift of the light spot (due to spacecraft motion) results in new pixels being illuminated and a different signal, (c) additional motion illuminates yet different pixels.

PRNU can be decomposed into two components. One is pixel-to-pixel (i.e. *inter*pixel) variation caused by changes in average quantum efficiency from one pixel to the next, and small variations in pixel size.[23] The second is *intra*pixel variation caused by changes in quantum efficiency on scales smaller than a single pixel.[24] PRNU

is typically addressed by flat-fielding the CCD, however ExoplanetSat lacks space for an internal flat-fielding source. In addition, flat-fielding cannot account for intrapixel variation. We expect jitter noise to be the limiting noise source. I.e. even in photon-noise dominated situations while observing bright stars over long integrations, jitter noise will still impose an upper bound on the achievable signal-to-noise ratio.

3.2.1 Simulation

In order to analyze the effect of jitter noise and derive a requirement for spacecraft pointing, we have created a physics-based simulation. Similar to numerical models developed for the MOST[17] and Kepler[25] missions, the ExoplanetSat simulation is used to conduct design trades and in the present case provides initial insights into feasibility. The simulation models diffraction using the standard Fourier transform relationship between the optical system pupil function and the incoherent point spread function (PSF). I.e.

$$h_{\mathrm{I}}(x', y') = |h(x', y')|^2 \tag{7}$$

where $h_{\mathrm{I}}(x', y')$ and $h(x', y')$ are the incoherent and coherent PSF, respectively. The later is given in the Fraunhofer limit by Fourier transforming the pupil mask and scaling to image coordinates (x', y'):

$$h(x', y') \propto G_{\mathrm{pupil}}\left(\frac{x'}{\lambda f}, \frac{y'}{\lambda f}\right)$$
$$= G_{\mathrm{pupil}}(u, v)\big|_{\left(\frac{x'}{\lambda f}, \frac{y'}{\lambda f}\right)} \tag{8}$$

where f is the focal length of the optical system, λ is the wavelength of light, and (u, v) are frequency components. Note that the the frequency components are related to the physical dimensions of the pupil via the Nyquist sampling relationships,

$$\frac{\Delta x}{\delta x} = \frac{2\Delta u}{\delta u} \equiv N_x \qquad \frac{\Delta y}{\delta y} = \frac{2\Delta v}{\delta v} \equiv N_y$$

where $\Delta x, \Delta y$ is the size of the pupil field, $\delta x, \delta y$ is the pupil sample size, $2\Delta u, 2\Delta v$ is the frequency bandwidth and $\delta u, \delta v$ is the frequency resolution in the horizontal and vertical directions, respectively.

Returning to the PSF, the Fourier transform of the pupil function (3) can be written more explicitly as,

$$G_{\mathrm{pupil}}(u, v) = \mathcal{F}\left[g_{\mathrm{pupil}}(x, y)\right] \tag{9}$$

where,

$$g_{\mathrm{pupil}}(x, y) = A_{\mathrm{pupil}}(x, y) \exp\{i\phi_{\mathrm{pupil}}(x, y)\} \tag{10}$$

is the complex pupil mask broken down into a spatially-dependent amplitude and phase functions $A(x, y)$ and $\phi(x, y)$. A top hat function of a size equal to the lens aperture is used as the amplitude function. The phase function is a combination of three terms: x-tilt, y-tilt, and defocus. The tilts are caused by errors in spacecraft pointing while the defocus is deliberately introduced in order to spread the incoming light over multiple pixels. Therefore the phase at the pupil is,

$$\phi(x, y) = \frac{2\pi}{\lambda}\left[\frac{1}{2}\delta z \frac{x^2 + y^2}{f^2} + (4.848137 \times 10^{-6})\theta_x x + (4.848137 \times 10^{-6})\theta_y y\right] \quad [\mathrm{rad}] \tag{11}$$

where δz is the amount by which the focal plane is moved out of focus, θ_x and θ_y are the x and y spacecraft pointing errors in arcseconds, f is the focal length, and λ is the observing wavelength. Equations (7) through (11) thus provide a means of generating a simulated image of the target star. After generating a PSF, the image is then re-sampled onto a detector with given quantization and noise characteristics (see Figure 7). For the purposes of this work, a PRNU of 1% is assumed and only interpixel variation is taken into account. Intrapixel variation will be considered in the future.

Jitter noise is a function of several system parameters, including the amplitude of jitter from the spacecraft reaction wheels and target star magnitude. Simulation is used to explore the effect of these parameters on meeting the 10 ppm science requirement. In order to isolate the effect of jitter, the CCD noise sources (read, photon, and dark current noise) are disabled. Simulation parameters are given in Table 2 and parameter-specific results are presented in the following sections. Note that the total observation time t_{obs} is fixed at 100 seconds. During each observation, there are a number of shorter integrations of length t_{int} that are co-added.

(a) Pupil phase (uniform, zero defocus)

(b) Broadband PSF

(c) PSF as sampled by detector (15 μm pixels)

(d) Pupil phase (quadratic, 70μm defocus)

(e) Broadband PSF

(f) PSF as sampled by detector (15 μm pixels)
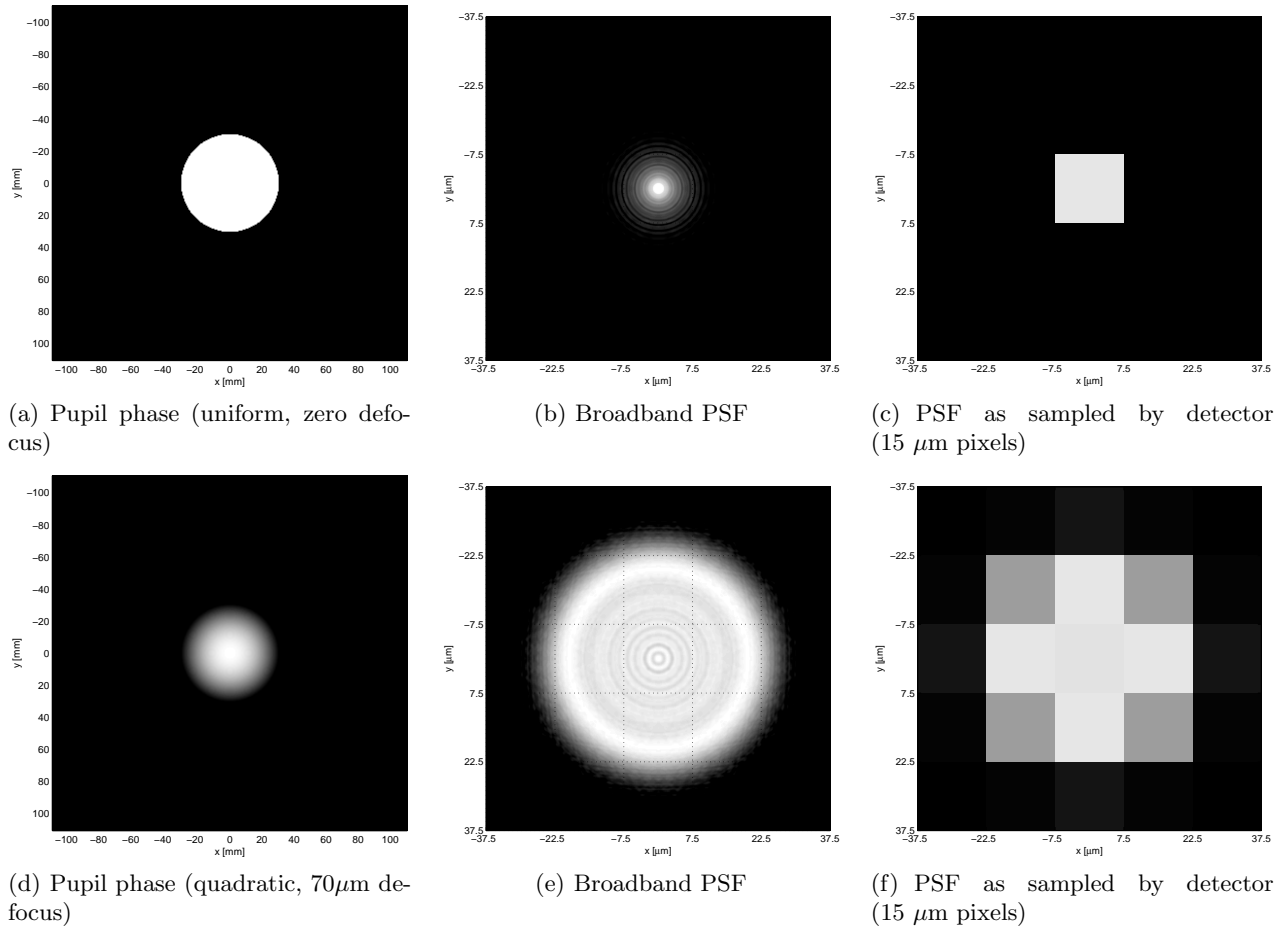
Figure 7. Sample simulation outputs for perfectly focused system (a-c) and defocused system (d-f). In these samples 400 nm $< \lambda <$ 900 nm and defocus is added via a quadratic phase term at the pupil (d).

Table 2. Simulation parameters.

Parameter	Symbol	Value	Units	Notes
Focal length	f	85	mm	
f-number	f/#	1.4	-	
Aperture diameter	D	60.7	mm	From focal length and f-number
Wavelength	λ	650	nm	Center of 400 - 900 nm bandpass
Pixel size		15	μm	
PRNU		1%	-	1σ
Quantization		16	bits	
Well capacity		100,000	e-	
Integration time	t_{int}	0.5	s	
Spot diameter	D_{spot}	35	pixels	
Observation time	t_{obs}	100	s	
Jitter amplitude	$\delta\theta_x,\delta\theta_y$	{0.1, 1, 10}	arcseconds	3σ
Target star V magnitude	M_V	0 - 7	-	

3.2.2 Results

The model discussed above was used to conduct Monte Carlo simulations of imaging in the presence of random pointing offsets due to reaction wheel jitter. These offsets have 3σ values $\delta\theta_x$ and $\delta\theta_y$ that are deliberately

varied to determine the effect of jitter on the photometric signal. Only interpixel PRNU was considered in this initial analysis; each pixel is assumed to have uniform quantum efficiency for the sake of computational efficiency. Figure 8(a) shows the simulated jitter motion of spot centroids superimposed on the scale of the focal plane. Figure 8(b) shows jitter noise as a function of stellar magnitude and pointing error.
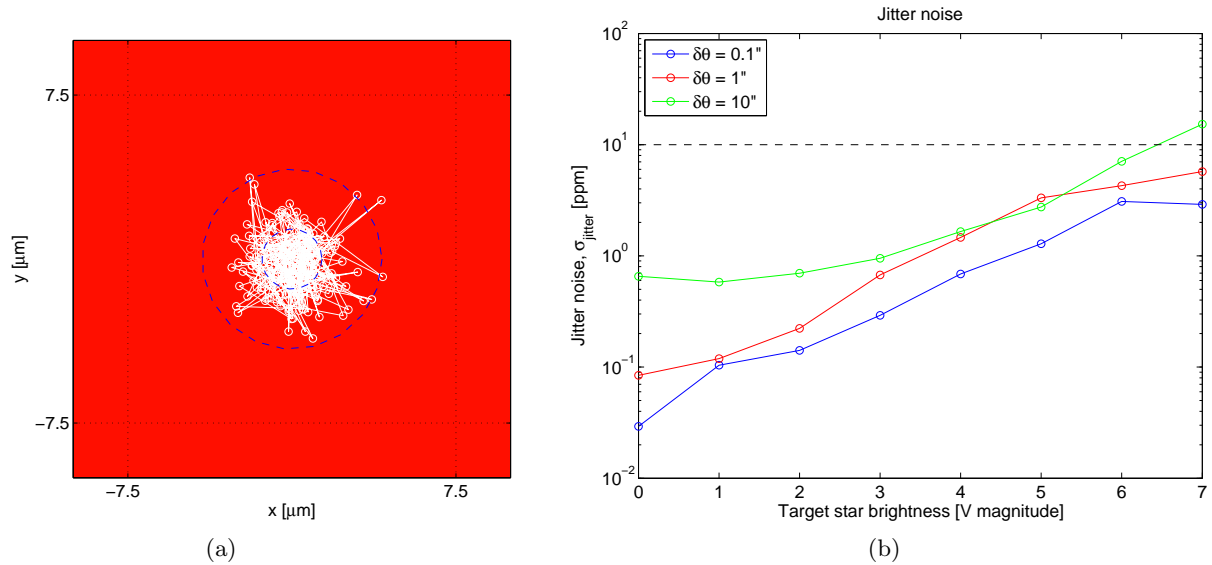

(a)   (b)

Figure 8. (a) Centroid motion on the focal plane due to spacecraft jitter with 1σ and 3σ circles drawn (note the relative size of the 15 μm pixels. (b) Jitter noise as a function of target star brightness M_V and 3σ jitter amplitude $\delta\theta$.

Figure 8(b) shows the expected trend wherein jitter noise increases for decreasing brightness. This is due to the fact that jitter noise is normalized by the signal when expressed in parts per million—brighter stars have lower relative noise. The lack of smoothness in the curves is due to the particular shape of the PSF used in the simulation. For computational efficiency, a monochromatic airy pattern was used in place of a broadband version. The internal structure present in the monochromatic PSF contributes to the peaks and troughs in the graph. The trend and noise values, however, remain valid. Figure 8(b) also shows that jitter noise increases for larger jitter amplitudes, which is expected as well. All points lie below the noise requirement except for the 10 arcsecond, 7th magnitude case. Given the constraints imposed by CCD noise (Figure 5), these jitter noise results show that pointing accuracies on the order of single arcseconds will be required by the attitude control subsystem to maintain the overall error budget (1) down to 4th magnitude.

3.2.3 Future jitter noise studies

This simulation currently takes into account only a subset of parameters that influence jitter noise. For example, it is suspected that spot size has an effect by changing the proportion of pixels at the edge of the spot in relation to the center (the edge pixels contribute to the changing signal which causes jitter noise). Likewise, the present simulation does not account for intrapixel variation, which has a potentially large contribution to jitter noise. In the absence of this within-pixel variation, the jitter noise seen in the above analysis is due primarily to the spot illuminating a different fraction of the pixels on the spot edge. When the spot moves, a new fraction of each edge pixel is illuminated, which causes signal variation (jitter noise) even with uniform intrapixel response.

4. CONCLUSION

This work presents an initial concept and baseline design for ExoplanetSat—a 3U CubeSat space telescope designed to monitor the brightest Sun-like stars for transiting Earth analogs. By adopting the CubeSat form factor, we aim to take advantage of low-cost piggyback launch opportunities and leverage existing COTS technologies. We present key subsystems, including a two-stage scheme for arcsecond-level pointing. The optical subsystem

uses a refractive SLR camera lens and composite focal plane for both science measurements and guide star tracking. An initial analysis of detector and jitter noise shows that the 10 ppm noise threshold—the minimum required for detecting Earth-like exoplanets—is achievable given sufficiently low dark current noise, high photon flux, and highly precise pointing at the 0.1 to 1 arcsecond level. While we have shown that the pointing requirement is within reach, these goals are extremely difficult to reach within the constraints of a CubeSat and will be developed further in future publications. The transit method is directly scalable to other planet-star area ratios for a given system noise level. Therefore if mass and volume constraints prove the 10 ppm requirement to be infeasible, the science requirement may be adjusted to focus on larger exoplanets.

4.1 Future work

A key element of any future work is expansion and maturation of the imaging simulation. The ultimate goal is to create an end-to-end numerical model that can be used to simulate transit events in the presence of all anticipated noise sources. Central to this modeling effort will be benchmarking the simulation against experimental measurements. We anticipate doing this using a jitter noise testbed currently under construction at MIT. It will provide a way to inject a known amount of jitter-induced focal plane motion and measure the resulting signal error.

An item that will receive particular attention is the issue of stray light from the Earth and Moon entering the telescope during science operations. Volume constraints prevent the use of a large baffle, therefore a detailed analysis must be undertaken to characterize the detrimental impact stray light will have on the ability to meet science requirements. This and other efforts will continue over the coming months to mature the ExoplanetSat design and develop a functional prototype.

REFERENCES

[1] des Marais, D. J., Harwit, M. O., Jucks, K. W., Kasting, J. F., Lin, D. N., Lunine, J. I., Schneider, J., Seager, S., Traub, W. A., and Woolf, N. J., "Remote sensing of planetary properties and biosignatures on extrasolar terrestrial planets," *Astrobiology* **2**(2), 153–181 (2002).

[2] White, M. L., Shaklan, S. B., Lisman, P., Ho, T., Mouroulis, P., Basinger, S. A., Ledeboer, W., Kwack, E.-Y., Kissil, A., Mosier, G. E., Liu, A., Bowers, C., and Blaurock, C., "Design and performance of the Terrestrial Planet Finder coronagraph," *Proc. SPIE* **5487**(1234) (2004).

[3] Lawson, P. R., Lay, O. P., Martin, S. R., Peters, R. D., Gappinger, R. O., Ksendzov, A., Scharf, D. P., Booth, A. J., Beichman, C. A., Serabyn, E., Johnston, K. J., and Danchi, W. C., "Terrestrial Planet Finder Interferometer: 2007-2008 progress and plans," *Proc. SPIE* **7013** (2008).

[4] Seager, S., Ford, E. B., and Turner, E. L., "Characterizing Earth-like planets with terrestrial planet finder," *Proc. SPIE* **4835**(79) (2002).

[5] Unwin, S. C. and Beichman, C. A., "Terrestrial Planet Finder: science overview," *Proc. SPIE* **5487**(1216) (2004).

[6] Charbonneau, D., Brown, T. M., Noyes, R. W., and Gilliland, R. L., "Detection of an Extrasolar Planet Atmosphere," *ApJ* **568**(1) (2002).

[7] Tinetti, G., Vidal-Madjar, A., Liang, M.-C., Benulieu, J.-P., Yung, Y., Carey, S., Barber, R. J., Tennyson, J., Ribas, I., Allard, N., Ballester, G. E., Sing, D. K., and Selsis, F., "Water vapour in the atmosphere of a transiting extrasolar planet," *Nature* **448**, 169–171 (2007).

[8] Swain, M. R., Vasisht, G., and Tinetti, G., "The presence of methane in the atmosphere of an extrasolar planet," *Nature* **452**, 329–331 (2008).

[9] Heidt, H., Puig-Suari, J., Moore, A. S., Nakasuka, S., and Twiggs, R. J., "CubeSat: A new generation of picosatellite for education and industry low-cost space experimentation," *14th Annual USU Conference on Small Satellites* **5** (2000).

[10] [*CubeSat Design Specification Rev. 12*], The CubeSat Program, Cal Poly San Louis Obispo (2009).

[11] Puig-Suari, J., Turner, C., and Ahlgren, W., "Development of the standard CubeSat deployer and a CubeSat class picosatellite," *Proc. IEEE Aerospace Conference* **1**, 347–353 (March 2001).

[12] Kalman, A., Reif, A., Berkenstock, D., Mann, J., and Cutler, J., "MISC–a novel approach to low-cost imaging satellites," *22nd Annual USU Conference on Small Satellites* **3** (2008).

[13] Klamper, A., "NRO Embraces Cubesats for Testing Advanced Technologies," *Space News Business Report* (August 13 2009).

[14] Viard, T., Bodin, P., Magnan, A., and Baglin, A., "CoRoT Telescope," *Proc SPIE* **6693** (2007).

[15] Auvergne, M., Bodin, P., Boisnard, L., Buey, J.-T., Chaintreuil, S., Epstein, G., and Jouret, M., "The CoRoT satellite in flight: description and performance," *Astronomy and Astrophysics* **506**, 411–424 (2009).

[16] Mayor, M., Naef, D., Pepe, F., Queloz, D., Santos, N., and Udry, S., "The Geneva Extrasolar Planet Search Programmes," *http://exoplanets.eu/* (2010).

[17] Walker, G., Matthews, J., Kusching, R., and Johnson, R., "The MOST Astroseismology Mission: Ultraprecise Photometry from Space," *Pub. Astron. Soc. Pac.* **115**, 1023–1035 (2003).

[18] Rowe, J. F., Matthews, J. M., Seager, S., Sasselov, D., Kusching, R., Guenther, D. B., Moffat, A. F. J., Rucinski, S. M., Walker, G. A. H., and Weiss, W. W., "Towards the Albedo of an Exoplanet: MOST Satellite Observations of Bright Transiting Exoplanetary Systems," *Proc. IAU Symposium* **258** (2008).

[19] Borucki, W. J., Koch, D. G., Lissauer, J. J., Basri, G. B., Caldwell, J. F., Cochran, W. D., Dunham, E. W., Geary, J. C., Latham, D. W., Gilliland, R. L., Caldwell, D. A., Jenkins, J. M., and Kondo, Y., "The Kepler Mission: A Wide Field of View Photometer Designed to Determine the Frequency of Earth-Size Planets Around Solar-Like Stars," *Proc. SPIE* **4854** (2003).

[20] Brady, T., *The HETE-II Primary Ground Station System and Electronics*, Master's thesis, Massachusetts Institute of Technology (1999).

[21] Pong, C. M., Lim, S., Smith, M. W., Miller, D. W., Villasenor, J. S., and Seager, S., "Achieving high-precision pointing on ExoplanetSat: Initial feasibility analysis," *Proc. SPIE* **7731**(68) (2010).

[22] Division, C. Z. C. L., "Photography in space," *Zeiss Camera Lens News* **33**, 8–9 (2009).

[23] Smith, R. M. and Rahmer, G., "Pixel area variation in CCDs and implication for precision photometry," *Proc. SPIE* **7021** (2008).

[24] Hardy, T., Baril, M. R., Pazder, J., and Stilburn, J. S., "Intra-pixel response of infrared detector arrays for JWST," *Proc. SPIE* **7021** (2008).

[25] Remund, Q. P., Jordan, S. P., Updick, T. F., Jenkins, J. M., and Borucki, W. J., "Kepler system numerical model for the detection of extrasolar terrestrial planets," *Proc. SPIE* **4495** (2002).